J. Fluid Mech. (2024), *vol*. 987, R5, doi:10.1017/jfm.2024.400

Divergent Richtmyer–Meshkov instability under different shock strengths

Juchun Ding[1], **Duo Zhang**[1] **and Xisheng Luo**[1],†

[1]Department of Modern Mechanics, University of Science and Technology of China, Hefei 230026, PR China

(Received 1 February 2024; revised 18 March 2024; accepted 18 April 2024)

Richtmyer–Meshkov (RM) instability at a single-mode interface impacted by a cylindrical divergent shock with low to moderate Mach numbers is investigated experimentally. The motion of an unperturbed interface is first examined to obtain the background flow. The shocked interface moves uniformly at the early stage, but later decelerates. The stronger the incident shock, the larger the interface deceleration, which is reasonably predicted by a one-dimensional model considering the effect of postshock non-uniformity. Such a deceleration greatly inhibits the growths of harmonics of an initially perturbed interface and, consequently, the divergent RM instability presents very weak nonlinearity from early to late stages. Particularly, higher-Mach-number cases present weaker nonlinearity due to larger deceleration there. This abnormal linear growth regime is reported for the first time. Benefiting from this, the incompressible linear model holds validity at all stages of divergent RM instability. It is also found that compressibility inhibits the initial growth rate, but produces a weak influence on the subsequent instability growth.

Key words: shock waves

1. Introduction

The growth of perturbations at an interface between two different fluids subjected to an impulsive acceleration is usually referred to as the Richtmyer–Meshkov (RM) instability, which was first analysed theoretically by Richtmyer (1960) and later confirmed experimentally by Meshkov (1969). Another similar hydrodynamic instability is the Rayleigh–Taylor (RT) instability (Rayleigh 1883; Taylor 1950), for which the interface suffers a finite, sustained acceleration. Although the RM and RT instabilities share the common evolution processes, such as the formation of bubbles and spikes as well as the flow transition to turbulent mixing, their underlying regimes are distinct. In recent decades, the RM instability has received increasing attention due to its significance in scientific research (e.g. compressible turbulence) (Noble *et al.* 2023) and practical applications

† Email address for correspondence: xluo@ustc.edu.cn

(e.g. supernova explosion) (Musci *et al.* 2020), and comprehensive reviews have been reported (Ranjan, Oakley & Bonazza 2011; Zhou 2017).

Compressibility and nonlinearity are two major obstacles to developing an accurate model for the RM instability (Wouchuk 2001). At the early stage when the transmitted and reflected waves are close to the interface, compressibility is dominant and nonlinearity is less important. As the waves are far away from the interface, compressibility is weak and nonlinearity becomes dominant. Hence, the RM instability experiences the transition from a linear compressible regime at the early stage to a nonlinear incompressible regime at the late stage. A combined model for the instability growth at the whole stage can be achieved by matching the compressible linear model (valid at the early stage) and the incompressible nonlinear model (valid at the late stage). This physical picture has been demonstrated true for the weak shock case (Zhang & Sohn 1997). However, for a moderate or strong shock, the transmitted shock (TS) is close to the interface for a long time and the transverse waves behind the shock continuously affect the interface evolution (called shock proximity effect), giving rise to an evident compressibility effect at late stages. This has been confirmed by several independent shock-tube experiments (Sadot *et al.* 2003; Puranik *et al.* 2004; Motl *et al.* 2009), in which the bubbles were observed to be flattened by the transverse waves at the late stage. The coexistence of compressibility and nonlinearity at late stages poses a great challenge for theoretical treatment.

Previous studies on compressibility effect mainly considered the RM instability induced by a planar shock with moderate to strong strengths. This is not the case in realities such as inertial confinement fusion (ICF) and supernova explosion, where the RM instability is usually induced by a curved shock. A typical example is the divergent shock. For example, the divergent RM instability is an important physical process that should be considered when explaining the remnant of supernova explosion. Also, in ICF, after the convergent shock focuses at the geometric centre, a reflected divergent shock is generated immediately, which later triggers the divergent RM instability, greatly enhancing the material mixing. The underlying regimes of the divergent RM instability are distinctly different from the planar and convergent counterparts. Specifically, geometric expansion inhibits the instability growth for incompressible flows. In addition, a divergent shock becomes weaker and weaker with time, and thus a non-uniform, unsteady flow field is established behind it (Zhang *et al.* 2023). Moreover, either nonlinearity or compressibility behaves differently in the divergent RM instability as it does in the planar and convergent cases. For these reasons, the divergent RM instability could present unique high-Mach-number effects, which motivates the present study. In this work, the influence of shock intensity on the divergent RM instability is investigated, focusing on the roles of compressibility and nonlinearity in the divergent RM instability, particularly for cases with higher Mach numbers.

Shock-tube experiments on the evolution of a well-characterized single-mode interface impacted by a cylindrical divergent shock with various Mach numbers are performed. An unperturbed interface is first examined to obtain the background flow. The effect of non-uniform pressure field behind the divergent shock on the interface motion is discussed and modelled. A thorough analysis on the effects of compressibility, nonlinearity and RT stabilization under various Mach numbers is presented. The result illustrates the existence of unique flow regimes for the divergent RM instability.

2. Experimental methods

The experiments are performed in a novel divergent shock tube designed based on shock dynamics theory. A sketch of the shock tube is given in figure 1(*a*). An initial planar

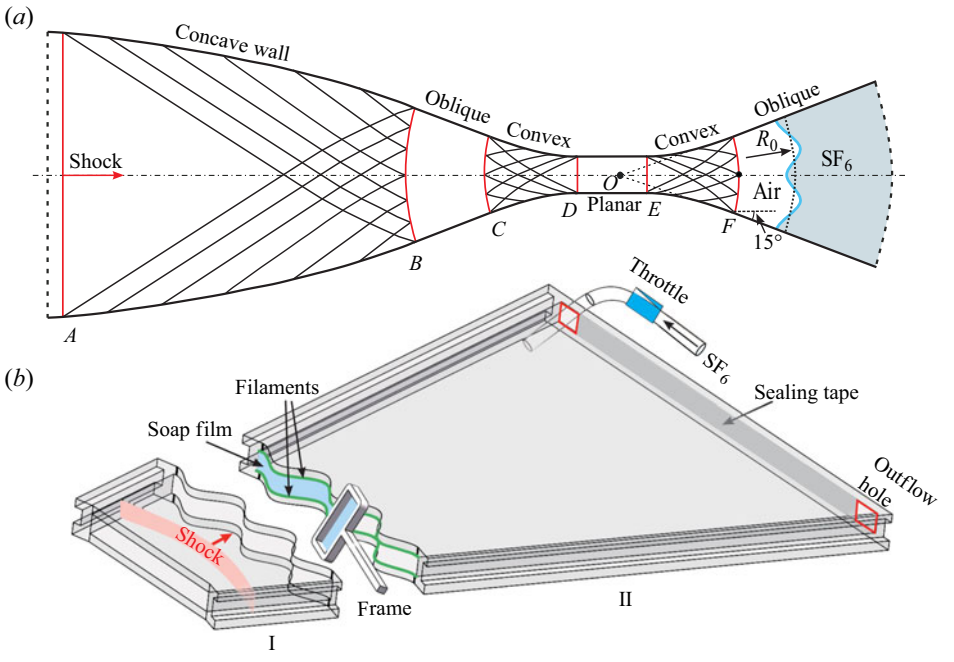

Figure 1. Schematic diagrams of (*a*) the shock tube and (*b*) the interface-formation device.

shock is generated immediately after the rupture of the diaphragm separating the driver and driven sections. When this planar shock propagates along the concave wall *AB*, it is transformed gradually to a cylindrical convergent shock. As time proceeds, the cylindrical shock converges along the oblique wall *BC* with its strength increasing gradually. Later, it is converted back into a planar shock by the convex wall *CD*. Note this planar shock is stronger than the initial one (Zhan *et al.* 2018). Subsequently, the strong planar shock is converted to a cylindrical divergent shock by the convex wall *EF*. Afterwards, the divergent shock collides with the downstream air/SF_6 interface, triggering the divergent RM instability. For more details about the design principle of the shock tube, readers are referred to previous works (Zhai *et al.* 2010; Li *et al.* 2020).

The gas interface is created with a well-verified soap-film technique that can largely eliminate initial imperfections at the interface including short-wavelength perturbations, diffusion layer and three-dimensionality (Liu *et al.* 2018). As depicted in figure 1(*b*), the interface is formed in a device composed of sections I and II. These two sections are made of transparent acrylic plates (3 mm thick) sculpted by a high-precision engraving machine. For section II, two grooves (0.75 mm deep and 0.5 mm wide) with the same shape as the desired interface are engraved on the internal surfaces of the upper and lower plates. Then, two thin filaments (1.0 mm high and 0.5 mm wide) with the same shape as the grooves are, respectively, inserted into the two grooves to produce desired constraints. The height of the filaments protruding into the flow is less than 0.3 mm, which is much smaller than the inner height (7.0 mm) of the test section, and thus produces a negligible influence on the flow. As a square frame dipped with moderate soap solution (60 % distilled water, 20 % sodium oleate and 20 % glycerine) is pulled along the filaments, a soap-film interface that presents the same shape as the filaments is generated. Subsequently, SF_6 gas is pumped into section II through the inflow hole to exhaust air through the outflow hole. An oxygen concentration detector is placed at the outflow hole to ensure a high concentration of SF_6 inside the layer.

Case	Ma	a_0-n	V_{ics} (m s^{-1})	ΔV (m s^{-1})	V_{ts} (m s^{-1})	mfra(SF_6)	A	$\dot{a}_0$ (m s^{-1})
U1	1.3	0–0	443.7	90.2	196.8	0.98	0.65	—
U2	1.4	0–0	485.1	123.8	219.2	0.99	0.67	—
U3	1.6	0–0	550.5	181.2	259.9	0.99	0.66	—
U4	1.7	0–0	603.0	209.7	288.9	0.99	0.66	—
S1	1.3	1.5–36	441.9	94.4	195.2	0.98	0.66	9.6
S2	1.4	1.5–36	485.1	118.0	219.8	0.99	0.67	10.2
S3	1.6	1.5–36	554.4	175.8	256.6	0.99	0.67	13.5
S4	1.7	1.5–36	598.5	200.0	289.0	0.98	0.66	16.8

Table 1. Detailed parameters corresponding to initial conditions for each case. Here a_0 and n are the initial amplitude and azimuthal mode number of the interface, respectively; V_{ics} is the incident shock velocity; V_{ts} is the transmitted shock velocity; ΔV is the initial velocity of the shocked interface; mfra(SF_6) is the mass fraction of SF_6 on the right side of the interface; A is the preshock Atwood number.

The initial conditions such as shock strength, interface shape and gas concentration can be well controlled in the experiment, which ensures high repeatability of the experimental results. In the cylindrical coordinate system, a single-mode interface can be parameterized as $r(\theta) = R_0 + a_0\cos(n\theta - \pi)$, where R_0 ($= 160$ mm) refers to the radius of the initial unperturbed interface, a_0 to the initial amplitude, n to the azimuthal mode number and θ to the azimuthal angle. This interface is sketched on the right side of figure 1(*a*), and the angle θ is measured from the origin O drawn in the segment labelled DE. The flow field is recorded by a high-speed schlieren system. The frame rate of the high-speed camera is set to be 60 000 f.p.s. with a shutter time 1 µs. The spatial resolution of schlieren images is 0.34 mm pixel^{-1}. The ambient pressure and temperature are 101.3 kPa and 296 ± 2 K, respectively.

3. Results and discussion

A quasi-1-D experiment corresponding to a uniform cylindrical interface interacting with a cylindrical divergent shock is first performed to examine the background flow, for which there is no theoretical solution. Various shock Mach numbers are considered. Detailed parameters corresponding to the initial conditions for cases U1-U4 are listed in table 1, where the Atwood number (A) is defined as $A = (\rho_2 - \rho_1)/(\rho_2 + \rho_1)$ with ρ_1 and ρ_2 being the gas densities on the left and right sides of the interface, respectively. Sequences of schlieren images illustrating the movements of the interface and the shock for cases U1 and U4 are displayed in figure 2. Case U1 is taken as an example to detail the motion process. Time origin in this work is defined as the moment at which the incident shock arrives at the mean position of the interface. At the beginning (-26 µs), an incident cylindrical shock (ICS) together with a cylindrical unperturbed interface (UI) is clearly observed. Later, the ICS collides with the air/SF_6 interface, bifurcating into an inward-moving reflected shock (RS) and an outward-moving TS (40 µs). After that, the shocked interface (SI) moves downstream following the TS. Due to the shock impact, the soap film is atomized into small droplets with a diameter of approximately 30 µm. Previous studies (Ding *et al.* 2017; Liu *et al.* 2018; Zhang *et al.* 2023) have demonstrated a negligible influence of the soap droplets on the interface evolution. The SI maintains a cylindrical shape during the experimental time, which indicates a negligible influence of boundary layer on the interface motion. The mass fraction of SF_6 inside the layer is determined based on 1-D gas dynamics theory, and the detailed estimation process has been reported by Zhang *et al.*

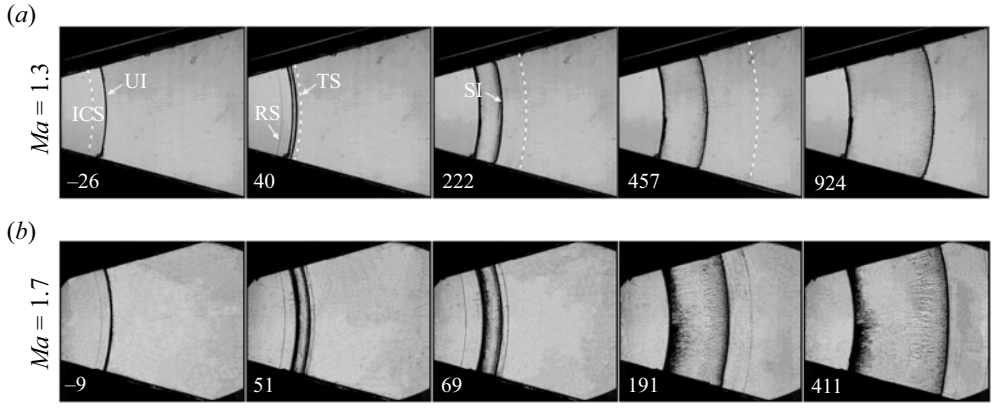

Figure 2. Schlieren images showing the motions of waves and the interface for cases U1 and U4: Ma, the Mach number of the incident shock; ICS, the incident cylindrical shock; UI, the initial unperturbed interface; SI, the shocked interface; TS, the transmitted shock; RS, the reflected shock. The unit of numbers is μs.

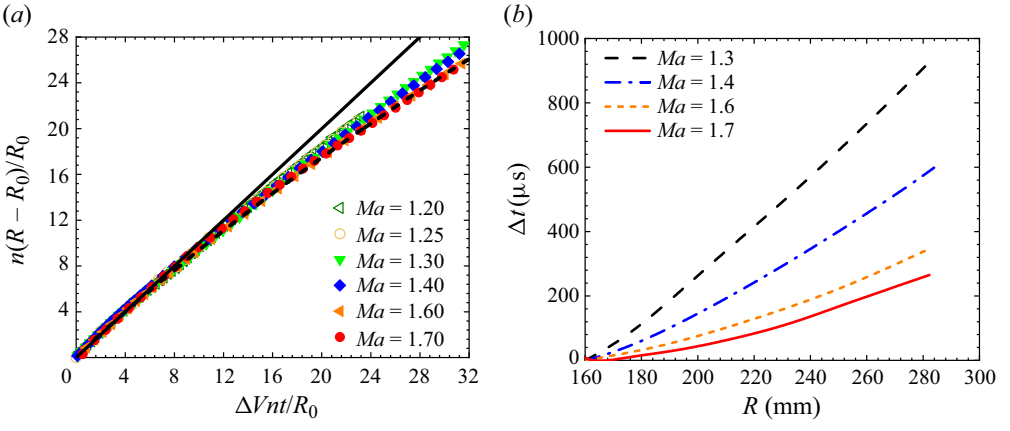

Figure 3. (*a*) Trajectories of the interface for all cases. (*b*) The time duration (Δt) between the moments at which the shock and the interface pass through position R.

(2023). It is found that as the shock is intensified, the relative velocity between the TS and the interface decreases, indicating a closer proximity between them.

Dimensionless variations of the interface displacement with time are plotted in figure 3(*a*), where two cases with lower Mach numbers reported by Li *et al.* (2020) are also given. Here, time is scaled as $\Delta Vnt/R_0$ with ΔV being the initial velocity of the SI and the interface displacement as $n(R-R_0)/R_0$ with R being the radius of the interface. For all cases, the interface moves uniformly during the early period following the shock passage, and later presents an evident deceleration. The stronger the incident shock, the larger the interface deceleration. The normalized trajectories of the interface collapse at the early stage for all cases, but deviate at the late stage due to different deceleration. It is desirable to derive an analytical solution for the interface trajectory, which is an important step towards the understanding and modelling of the divergent RM instability. Unfortunately, the unsteady, non-uniform flow behind the divergent shock greatly impedes the theoretical derivation.

In our recent work, an analytical solution for the trajectory of a fluid element in divergent geometry was derived under the incompressible flow assumption, which is expressed as

$$r = [r_0^2 + 2C(t - t_0)]^{1/2}. \tag{3.1}$$

Here t_0 is the initial time, $r_0 = r(t_0)$ and $C = u_0 r_0$ with $u_0 = u(t_0)$, where u is the flow velocity in the radial direction. Note the non-uniform postshock pressure field has not been taken into account in (3.1). Here, provided the initial shock strength $M = M_0$ at $r = r_0$, the variation of the divergent shock Mach number with radius r can be calculated according to the Chester–Chisnell–Whitham relation (Whitham 1958). To quantify the effect of a non-uniform pressure field on the interface motion, an assumption that the postshock pressure gradient remains invariant at each radius is adopted. Incorporating the pressure gradient (calculated by Rankine–Hugoniot conditions) into the 1-D momentum equation in a cylindrical coordinate system, the interface trajectory predicted by (3.1) can be modified. It is found that this modified model gives a reasonable prediction of the interface trajectory for all cases. Particularly, higher-Mach-number cases ($Ma = 1.6$ and 1.7) present better agreement with the prediction. An interpretation is given below. Figure 3(b) gives the time duration (Δt) between the instances at which the divergent shock and the SI pass through the position R. A notable reduction in Δt is observed when increasing the Mach number. It means that for a stronger shock, the postshock flow at radius R undergoes a shorter period of variation before the arrival of the interface. This makes the assumption of invariance of postshock pressure gradient more reasonable.

The divergent RM instability at a single-mode interface under four shock strengths (cases S1–S4) is then examined. Detailed parameters corresponding to the initial conditions for each case are listed in table 1. The initial amplitude of the interface is $a_0 = 1.5$ mm and the azimuthal mode number is $n = 36$, corresponding to an amplitude-to-wavelength ratio of 0.054. The other initial conditions remain the same as the unperturbed case. Developments of the wave patterns and the interface for these cases are illustrated in figure 4. Case S1 ($Ma = 1.3$) is taken as an example to detail the evolution process. At the beginning ($-9\,\mu$s), an ICS together with a sinusoidal perturbed interface (PI) are clearly observed. Then, the ICS collides with the PI, bifurcating immediately into sine-like transmitted and RSs (41 μs). During this process, the interface suffers a quick drop in amplitude due to shock compression. Subsequently, the SI moves downstream with its amplitude increasing persistently. As time proceeds, the TS propagates forwards with a gradually decaying amplitude and finally recovers to a uniform cylindrical shock (491 μs). It is worth noting that no evident spike and bubble structures are observed even at the late stage when intensifying the incident shock, which differs from the planar RM instability (Sadot *et al.* 2003; Motl *et al.* 2009). This phenomenon exists uniquely in divergent RM instability.

Normalized variations of the interface amplitude with time for all cases are plotted in figure 5(a). The amplitude is normalized as $\alpha = n(a - a_0^+)/R_0$ and the time as $\tau = n\dot{a}_0(t - t_0^+)/R_0$, where a_0^+ refers to the postshock amplitude, t_0^+ to the time just after the shock passage and $\dot{a}_0$ to the initial growth rate. The solid line in figure 5(a) refers to the linear prediction of Bell (1951) and the dashed line to the prediction of Epstein (2004) considering compressibility effect. The present experiments afford a longer observation time for the interface development as compared with that of Li *et al.* (2020) such that the instability growth at a later stage can be examined. The amplitude variation curves for these cases collapse quite well at the early stage, but deviate from each other at $\tau > 1.0$. For all cases, the growth rate decays gradually with time. The stronger the incident shock, the quicker the growth rate decay. Particularly, for the $Ma = 1.6$ and $Ma = 1.7$ cases, the

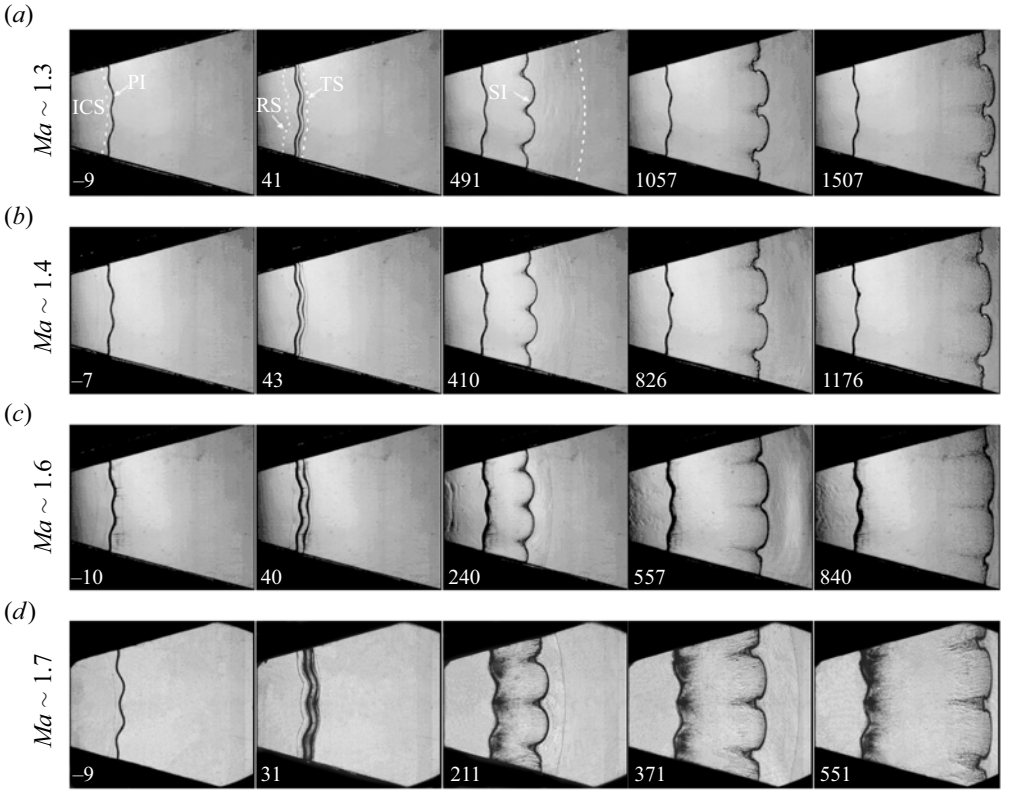

Figure 4. The developments of wave patterns and interfacial morphologies for all cases. The symbols are the same as those in figure 2. The unit of the numbers is μs.

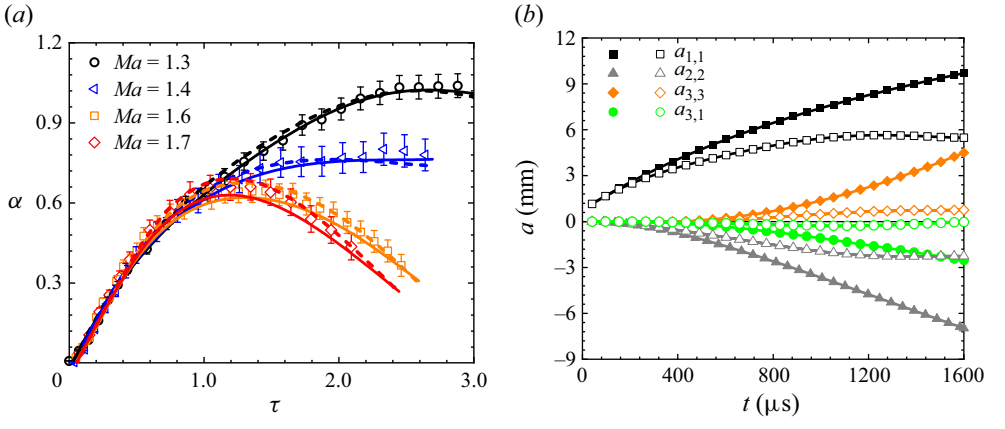

Figure 5. (*a*) Temporal variations of the interface amplitude and (*b*) comparison between the nonlinear predictions (Wang *et al.* 2015) considering uniform motion (filled symbol) and deceleration (hollow symbol) for harmonic growths. The solid line in (*a*) refers to the linear prediction of Bell (1951) and the dashed line to the prediction of Epstein (2004) considering compressibility effect.

interface amplitude decreases at the late stage (i.e. a negative growth rate), which indicates the presence of some factors stabilizing the instability.

The initial growth rates, obtained with a linear fit of experimental data, are 9.6, 10.2, 13.5 and 16.4 m s^{-1} for cases S1, S2, S3 and S4. The growth rates predicted by the

incompressible linear model (Bell 1951) are 16.1, 21.2, 28.6 and 47.0 m s^{-1} for cases S1–S4, respectively. The lower growth rate in experiment than prediction is primarily attributed to compressibility effect (i.e. pressure disturbances behind the reflected and TSs play a role). This is similar to the finding in convergent RM instability (Ding *et al.* 2017). Differing from the weak shock case, in which compressibility effect is weak at late stages, for a moderate shock ($Ma = 1.6$ and 1.7), the TS is closer to the interface (observed in the unperturbed case) and compressibility may be pronounced at late stages. Thus, the effect of compressibility on the instability growth is first assessed. Assuming the fluids on both sides of the interface are inviscid and irrotational and also undergo uniform compression (i.e. $\dot{\rho}_2/\rho_2 = \dot{\rho}_1/\rho_1$ with $\dot{\rho}_1(\dot{\rho}_2)$ being the first derivative of $\rho_1(\rho_2)$ with time), Epstein (2004) proposed a linear model for the instability growth at a perturbed cylindrical interface:

$$\left(-\frac{\dot{\rho}}{\rho} + \frac{\mathrm{d}}{\mathrm{d}t}\right)\frac{\mathrm{d}}{\mathrm{d}t}(a\rho R) = nAa\rho\frac{\mathrm{d}^2R}{\mathrm{d}t^2}, \tag{3.2}$$

where $\dot{\rho}/\rho = \dot{\rho}_2/\rho_2 \approx \dot{\rho}_1/\rho_1$ with ρ being the average density of fluids on both sides of the interface, and α is the amplitude of the perturbed interface. Letting $c = -\dot{\rho}/\rho$, the above formula is simplified to

$$\frac{\mathrm{d}^2a}{\mathrm{d}t^2} + \left(\frac{2\dot{R}}{R} - c\right)\frac{\mathrm{d}a}{\mathrm{d}t} - \left[(nA-1)\frac{\ddot{R}}{R} + \frac{\dot{R}}{R}c + \frac{\mathrm{d}c}{\mathrm{d}t}\right]a = 0. \tag{3.3}$$

Here, $R(t)$ is given by the function fitted from the measured radius of the corresponding UI, $\dot{R}$ and $\ddot{R}$ are the first and second derivatives of interface radius with time, respectively. For $c = -\dot{\rho}/\rho = 0$, the equation reduces to the Bell (1951) model for incompressible fluids. Here, the volume enclosed by the shock and the interface can be measured from schlieren images and thus the density variation rate c is available. Then, substituting the postshock parameters into (3.3), the instability growth with compressibility effect is obtained. As shown in figure 5(*a*), both compressible and incompressible models give a reasonable prediction of the instability growth within the measurement error. The predictions of the two models nearly collapse, which indicates a weak influence of compressibility on the instability growth for the parameter space considered in this work. Thus, the incompressible model is suitable for the present experiments. Note disturbances at a divergent shock decay more quickly than the convergent and planar shocks, which is a reason for the weak compressibility effect here.

Previous studies (Li *et al.* 2020; Zhang *et al.* 2023) showed that, in addition to the common regimes in planar RM instability, the growth of divergent RM instability at the linear stage is also affected by geometric divergence and RT effect. It is realized that these two effects could also affect the nonlinear growth of divergent RM instability, which has never been reported. To quantify the degree of nonlinearity, the growths of harmonics are obtained by performing the Fourier analysis of the interface morphologies extracted from the schlieren images. The Fourier analysis, which is applicable only to interfaces represented as single-valued functions, becomes invalid at the late stage when the spikes roll up. To obtain as much data as possible, the small curled structures at the spike head are removed via postprocessing. In this way, the growths of harmonics at a relatively later time can be obtained. As shown in the inserts of figure 6(*a*), a virtual interface composed of the first three harmonics obtained nearly collapses with the extracted morphology, which demonstrates the reliability of the Fourier analysis. Temporal variations of the amplitudes of the first three harmonics are plotted in figure 6. Higher-order harmonics that present a negligibly small amplitude during the experimental time are ignored. For cases S1

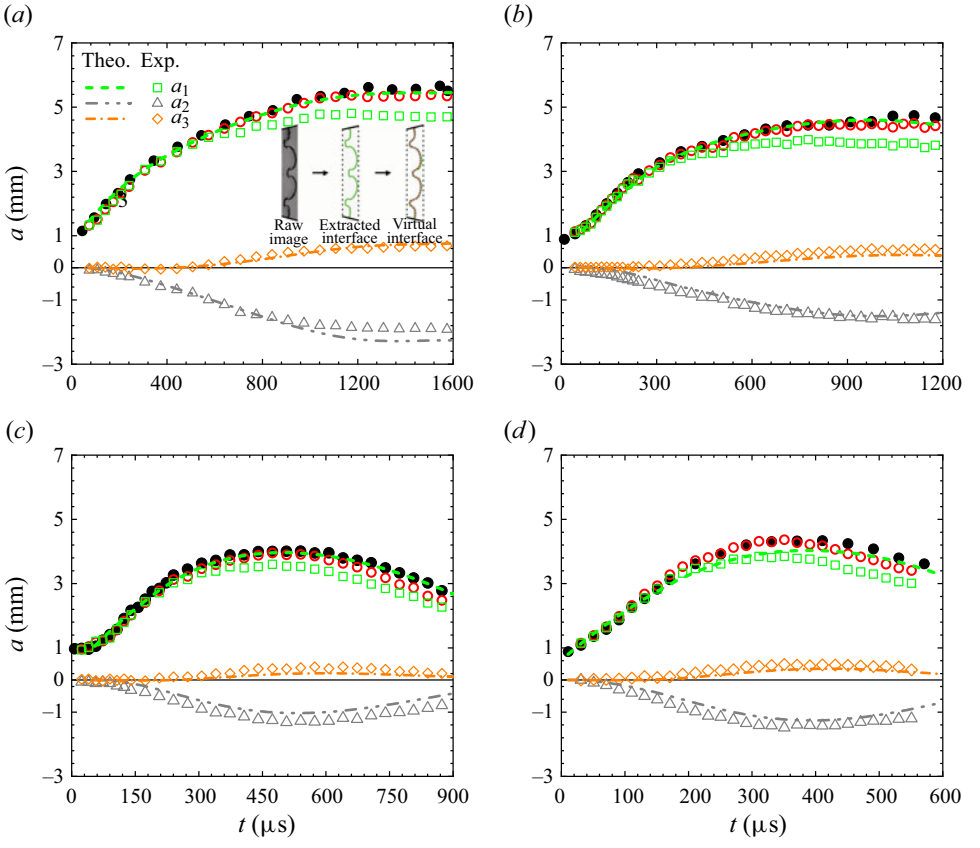

Figure 6. Comparisons between the experiment and the nonlinear prediction for the growths of the first three harmonics (a_1, a_2 and a_3) for cases S1 (*a*), S2 (*b*), S3 (*c*) and S4 (*d*). Filled symbols denote the amplitude of interface in experiment and hollow symbols denote the amplitude of a virtual interface composed of the first three harmonics.

and S2 ($Ma = 1.3, 1.4$), the amplitude of each harmonic increases persistently with a gradually decaying growth rate at the early stage and later freezes out. For cases S3 and S4 ($Ma = 1.6, 1.7$), the amplitude of each harmonic drops after saturation. The considerable amplitude of the second and third harmonics suggests that the instability has entered into a nonlinear stage. The freeze-out or decay of the second and third harmonics at the late stage indicates that nonlinearity is suppressed by a certain factor, particularly evident in stronger shock cases. The interface amplitude measured from experiment (filled circle) and that of the virtual interface composed of the harmonics (hollow circle) are also given in figure 6, and they collapse well.

Under the incompressible, inviscid, irrotational fluid assumption, a third-order weakly nonlinear model has been derived by Wang *et al.* (2015). Nevertheless, it is difficult to derive an analytical solution for the nonlinear growth of divergent RM instability at an interface with arbitrary radial motion. In this work, to predict the nonlinear growths of harmonics, the model of Wang *et al.* (2015) is solved numerically by substituting the parameters in the corresponding unperturbed case (i.e. displacement R, velocity $\dot{R}$ and acceleration $\ddot{R}$) into the model. Comparisons of the growths of harmonics between the experiment and the nonlinear prediction considering interface deceleration are given in figure 6. The model predicts well the growths of the second and third harmonics for

all cases. Also, it gives a good prediction of the first harmonic at the early stage, but overestimates the late-stage growth. A possible reason is that the prediction of the first harmonic takes only the third-order feedback into account, and higher-order harmonics are ignored. Both the freeze-out (cases S1 and S2) and amplitude reduction (cases S3 and S4) of the harmonics are well reproduced by the nonlinear model. To elucidate this phenomenon, comparison between the nonlinear predictions considering uniform (i.e. $\ddot{R} = 0$) and non-uniform motions for case S1 is made. As illustrated in figure 5(*b*), the interface deceleration greatly inhibits the growth of each harmonic, which manifests the significant role of RT effect in divergent RM instability, leading to very weak nonlinearity during the whole experimental time. Particularly, higher-Mach-number cases present weaker nonlinearity due to stronger RT effect there. This is consistent with the observation in schlieren images, where a distinct vortex pair is noticeable at the spike tip for cases S1–S2, but diminishes for cases S3–S4. This abnormal linear growth regime has never been discovered. Various decelerations in cases S1–S4 cause different degrees of suppression of the amplitude growth, which explains the deviation in amplitude growth among these cases (figure 5*a*). Note without interface deceleration (i.e. RT stability), the cylindrical RM instability could present evident nonlinearity (Matsuoka & Nishihara 2006). Under the incompressible flow assumption, geometric divergence causes a gradual reduction in interface amplitude and a continuous increment in wavelength, resulting in a low amplitude–wavelength ratio. This is also an important factor responsible for the longer linear stage observed in divergent RM instability than the planar and convergent counterparts. Despite the linear regime, geometric divergence effect that is inherent in divergent RM instability causes a continuous decay in growth rate, and thus the amplitude growth is no longer linear in time as in the planar RM instability. The present analysis gives an in-depth understanding of the regimes of divergent RM instability. The finding indicates that the coexistence of compressibility and nonlinearity at late stages of RM instability under strong shocks, that poses a great challenge to theoretical treatment, can be avoided for the divergent situation. This is crucial for modelling the divergent RM instability under strong shocks.

4. Conclusions

This work reports the shock-tube experiments on the divergent RM instability at a single-mode air/SF_6 interface under four Mach numbers. The cylindrical divergent shock is generated in a novel shock tube designed based on shock dynamics theory. The single-mode interface is created with an advanced soap-film technique. The unperturbed case is first examined to obtain the background flow. It is found that the interface moves uniformly at the early stage, and subsequently decelerates. The stronger the incident shock, the larger the interface deceleration. An approximate 1-D model considering the postshock pressure field reasonably predicts the interface trajectory. The divergent RM instability at a single-mode interface is then examined. It is found that compressibility effect inhibits the initial growth rate, but produces a negligible influence on the subsequent instability growth. By performing the Fourier analysis of the interface morphologies extracted from schlieren images, the growths of harmonics are obtained. For low Mach numbers, the amplitude of each harmonic increases persistently with a gradually decaying growth rate at the early stage and later freezes out. For moderate Mach numbers, the amplitude of each harmonic suffers a quick drop after saturation. The RT effect associated with interface deceleration provides a substantial inhibition on the growths of harmonics. As a result, the divergent RM instability presents very weak nonlinearity at the whole stage. Particularly, higher-Mach-number cases present weaker nonlinearity due to stronger RT effect there.

Reasonable agreement between the experiment and the nonlinear prediction of Wang *et al.* (2015) considering RT effect for the growths of the first three harmonics is obtained, which confirms the present analysis. The present finding provides deep insights into the regimes of divergent RM instability.

Funding. This work was supported by the National Natural Science Foundation of China (nos. 12072341, 12122213 and 12388101), the National Key Research and Development Program of China (2022YFF0504500) and the Strategic Priority Research Program of Chinese Academy of Science (XDB0500301).

Declaration of interests. The authors report no conflict of interest.

Author ORCIDs.
Juchun Ding https://orcid.org/0000-0001-6578-1694;
Xisheng Luo https://orcid.org/0000-0002-4303-8290.

References

Bell, G.I. 1951 Taylor instability on cylinders and spheres in the small amplitude approximation. *Rep. No. LA-1321* 1321. LANL.

Ding, J., Si, T., Yang, J., Lu, X., Zhai, Z. & Luo, X. 2017 Measurement of a Richtmyer–Meshkov instability at an air-SF_6 interface in a semiannular shock tube. *Phys. Rev. Lett.* **119** (1), 014501.

Epstein, R. 2004 On the Bell–Plesset effects: the effects of uniform compression and geometrical convergence on the classical Rayleigh–Taylor instability. *Phys. Plasmas* **11** (11), 5114–5124.

Li, M., Ding, J., Zhai, Z., Si, T., Liu, N., Huang, S. & Luo, X. 2020 On divergent Richtmyer–Meshkov instability of a light/heavy interface. *J. Fluid Mech.* **901**, A38.

Liu, L., Liang, Y., Ding, J., Liu, N. & Luo, X. 2018 An elaborate experiment on the single-mode Richtmyer–Meshkov instability. *J. Fluid Mech.* **853**, R2.

Matsuoka, C. & Nishihara, K. 2006 Fully nonlinear evolution of a cylindrical vortex sheet in incompressible Richtmyer–Meshkov instabilitys. *Phys. Rev.* E **73**, 055304.

Meshkov, E.E. 1969 Instability of the interface of two gases accelerated by a shock wave. *Fluid Dyn.* **4**, 101–104.

Motl, B., Oakley, J., Ranjan, D., Weber, C., Anderson, M. & Bonazza, R. 2009 Experimental validation of a Richtmyer–Meshkov scaling law over large density ratio and shock strength ranges. *Phys. Fluids* **21**, 126102.

Musci, B., Petter, S., Pathikonda, G., Ochs, B. & Ranjan, D. 2020 Supernova hydrodynamics: a lab-scale study of the blast-driven instability using high-speed diagnostics. *Astrophys. J.* **896** (2), 92–104.

Noble, C., Ames, A., McConnell, R., Oakley, J., Rothamer, D. & Bonazza, R. 2023 Simultaneous measurements of kinetic and scalar energy spectrum time evolution in the Richtmyer–Meshkov instability upon reshock. *J. Fluid Mech.* **975**, A39.

Puranik, P.B., Oakley, J.G., Anderson, M.H. & Bonazza, R. 2004 Experimental study of the Richtmyer–Meshkov instability induced by a Mach 3 shock wave. *Shock Waves* **13**, 413–429.

Ranjan, D., Oakley, J. & Bonazza, R. 2011 Shock-bubble interactions. *Annu. Rev. Fluid Mech.* **43**, 117–140.

Rayleigh, Lord 1883 Investigation of the character of the equilibrium of an incompressible heavy fluid of variable density. *Proc. Lond. Math. Soc.* **14**, 170–177.

Richtmyer, R.D. 1960 Taylor instability in shock acceleration of compressible fluids. *Commun. Pure Appl. Maths* **13**, 297–319.

Sadot, O., Rikanati, A., Oron, D., Ben-Dor, G. & Shvarts, D. 2003 An experimental study of the high Mach number and high initial-amplitude effects on the evoltion of the single-mode Richtmyer–Meshkov instability. *Laser Part. Beams* **21**, 341–346.

Taylor, G. 1950 The instability of liquid surfaces when accelerated in a direction perpendicular to their planes. I. *Proc. R. Soc. Lond.* A **201**, 192–196.

Wang, L.F., Wu, J.F., Guo, H.Y., Ye, W.H., Liu, J., Zhang, W.Y. & He, X.T. 2015 Weakly nonlinear Bell–Plesset effects for a uniformly converging cylinder. *Phys. Plasmas* **22**, 082702.

Whitham, G.B. 1958 On the propagation of shock waves through regions of non-uniform area or flow. *J. Fluid Mech.* **4**, 337–360.

Wouchuk, J.G. 2001 Growth rate of the linear Richtmyer–Meshkov instability when a shock is reflected. *Phys. Rev.* E **63**, 056303.

ZHAI, Z., LIU, C., QIN, F., YANG, J. & LUO, X. 2010 Generation of cylindrical converging shock waves based on shock dynamics theory. *Phys. Fluids* **22**, 041701.

ZHAN, D., LI, Z., YANG, J., ZHU, Y. & YANG, J. 2018 Note: A contraction channel design for planar shock wave enhancement. *Rev. Sci. Instrum.* **89**, 056104.

ZHANG, D., DING, J., SI, T. & LUO, X. 2023 Divergent Richtmyer–Meshkov instability on a heavy gas layer. *J. Fluid Mech.* **959**, A37.

ZHANG, Q. & SOHN, S.I. 1997 Nonlinear theory of unstable fluid mixing driven by shock wave. *Phys. Fluids* **9**, 1106–1124.

ZHOU, Y. 2017 Rayleigh–Taylor and Richtmyer–Meshkov instability induced flow, turbulence, and mixing. I. *Phys. Rep.* **720–722**, 1–136.